

Article

Kinetic and Isotherm Studies of Ni²⁺ and Pb²⁺ Adsorption from Synthetic Wastewater Using *Eucalyptus camdulensis*—Derived Biochar

Muhammad Shafiq ¹, Abdulrahman Ali Alazba ^{1,2} and Muhammad Tahir Amin ^{1,3,*}

¹ Alamoudi Water Research Chair, King Saud University, P.O. Box 2460, Riyadh 11451, Saudi Arabia; msrana@ksu.edu.sa (M.S.); alazba@ksu.edu.sa (A.A.A.)

² Agricultural Engineering Department, King Saud University, P.O. Box 2460, Riyadh 11451, Saudi Arabia

³ Department of Environmental Sciences, Abbottabad Campus, COMSATS University, Islamabad, Abbottabad 22060, Pakistan

* Correspondence: mtamin@ksu.edu.sa; Tel.: +966-11-467-3737

Abstract: The production of biosorbents by waste biomass has attracted considerable attention due to the low cost and abundance of the raw materials. Here biochar produced from *Eucalyptus camdulensis* sawdust (*EU*-biochar) via pyrolysis at 600 °C was used as a potential biosorbent for Ni²⁺ and Pb²⁺ metal ions from wastewater. Characterization experiments indicated the formation of C- and O-bearing functional groups on the *EU*-biochar surface, while shifts and changes in the shape of C–H bands suggested the adsorption of Ni²⁺ and Pb²⁺ onto *EU*-biochar by interacting with surface carboxylic groups. Pb²⁺ was adsorbed more quickly than Ni²⁺, indicating a faster and stronger interaction of Pb²⁺ with *EU*-biochar compared to Ni²⁺. As the initial concentrations of both metal ions increased, the percentage removal decreased, whereas increasing the *EU*-biochar dose improved the percentage removal but impaired the adsorption capacity for Ni²⁺ and Pb²⁺. The adsorption capacity could only be improved without affecting the percentage removal of both ions by increasing the pH of the metal solutions. The sorption efficiency of *EU*-biochar and the removal mechanism of Ni²⁺ and Pb²⁺ were further explored using non-linear and linear forms of kinetic and isotherm models.

Keywords: adsorption capacity; biochar; *Eucalyptus camdulensis*; removal mechanism; heavy metals; removal efficiency; kinetic model; isotherm model



Citation: Shafiq, M.; Alazba, A.A.; Amin, M.T. Kinetic and Isotherm Studies of Ni²⁺ and Pb²⁺ Adsorption from Synthetic Wastewater Using *Eucalyptus camdulensis*—Derived Biochar. *Sustainability* **2021**, *13*, 3785. <https://doi.org/10.3390/su13073785>

Academic Editor: Franco Marsan

Received: 18 February 2021

Accepted: 24 March 2021

Published: 29 March 2021

Publisher's Note: MDPI stays neutral with regard to jurisdictional claims in published maps and institutional affiliations.



Copyright: © 2021 by the authors. Licensee MDPI, Basel, Switzerland. This article is an open access article distributed under the terms and conditions of the Creative Commons Attribution (CC BY) license (<https://creativecommons.org/licenses/by/4.0/>).

1. Introduction

Rapid industrialization and urbanization in the last century have increased the consumption of global freshwater by six times [1], leading to a shortage of fresh drinking water for the majority of the world's population [2]. It is estimated that almost 3.9 billion people will suffer from water scarcity by 2050 [3]. Anthropogenic activities have also increased the levels of unwanted contaminants in freshwater resources worldwide [4]. For instance, industrial effluents carrying various organic and inorganic pollutants contribute significantly to the contamination and depletion of freshwater reservoirs [5]. In particular, metal and metalloids, such as nickel (Ni²⁺) and lead (Pb²⁺), are critical ecological threats, as they are widely used in plating and tanning, mineral, machinery, battery manufacturing, and other industries [6], while the Ni²⁺- and Pb²⁺-rich industrial effluents are discharged into adjacent water resources, posing a serious threat to human and animal health. In order to address the current challenges of increasing freshwater needs, depletion of available freshwater supplies, and deterioration of clean water resources due to contamination, numerous studies have focused on developing novel technologies for removing threatening pollutants from wastewater streams.

Specifically, several methods have been developed for the removal of metal and metalloids from wastewater streams, but most of them are ineffective or expensive. Even

advanced methods, such as catalytic degradation, oxidation, solvent extraction, membrane filtration, steam stripping, ion exchange, chemical precipitation, electrocoagulation, microbial degradation, and electrocoagulation, proved to be ineffective in completely removing contaminants from water [7–12]. In contrast, adsorption is a widely accepted technology for the removal of metal and metalloids from contaminated wastewater, as it is a cost-effective, highly efficient, and easy-to-use method that generates little residue and allows the recovery and recycling of the adsorbent unlike most traditional wastewater treatment methods [13,14]. Therefore, great effort has been made to develop effective, inexpensive, and environmentally friendly adsorbents that are suitable for each type of contaminant [15–18]. To date, several adsorbents, including clay, biomass, nanomaterials, layered double hydroxide, graphene, activated carbon, chitosan, and fly ash, have been successfully used for the removal of metal/metalloids from contaminated wastewater [19–27]. Furthermore, the production of biosorbents by reusing or recycling waste biomass and feedstock, such as agricultural waste and wood sawdust, has attracted considerable attention due to the low cost, abundance, and environmental friendliness of the raw materials [28–31]. Similarly, biochar has been produced from agricultural waste and used as an efficient adsorbent.

Biochar is a solid, black, and stable porous carbonaceous material produced by the pyrolysis of waste materials, such as wood, grass, manure, sludge, etc. [32], with little or no air at 300–800 °C [33,34]. Several studies have shown that biochar is one of the most effective adsorbents for the removal of metal or metalloids from industrial effluents due to its large specific surface area, water insolubility, richness in carbon, abundant pore structure, and active functional groups on its surface [35]. Moreover, the use of agricultural or fruit waste as the raw material not only reduces the overall costs, but also limits the pollution of surface water through the reuse of solid waste. To date, various waste materials, such as rice husk, wheat straw, wood waste biomass, and fruit waste, have been used to produce biochar to remove metals or metalloids from contaminated wastewater [29,36–40].

Based on the existing data, we considered that *Eucalyptus camdulensis* (EU) wood biomass could serve as a low-cost raw material for the production of biochar, as its extensive use in the manufacture of furniture and other purposes generates a large amount of sawdust waste. Therefore, in this study, we used EU sawdust to produce biochar via pyrolysis (EU-biochar), which was further evaluated as a potential adsorbent of Ni²⁺ and Pb²⁺ in synthetic contaminated water. In addition, we applied a series of kinetic and isotherm models to study the adsorption efficiency of EU-biochar and to elucidate the removal mechanism of Ni²⁺ and Pb²⁺ from water.

2. Materials and Methods

2.1. Preparation and Characterization of *Eucalyptus camdulensis* (EU)-Biochar

EU-biochar was prepared from EU sawdust collected from different places in Riyadh, Saudi Arabia. The collected sawdust was first washed with tap water to remove dirt particles, followed by pre-drying under sunlight for a few days, and final drying in an ordinary oven at 60 °C for 6 h. Small pieces of the oven-dried sawdust was then crushed to achieve an average particle size of about 0.5 mm. The very small pieces of EU sawdust were finally pyrolyzed in a box furnace (Nabertherm, B–150, Lilienthal, Germany) at 600 °C for 3 h to obtain EU-biochar with an average particle size of 50 µm. The specific surface area of EU-biochar was measured by Brunauer—Emmett—Teller analysis, while the carbon and volatile contents were estimated by proximate and ultimate analysis using an elemental analyzer (Thermo Fisher Scientific, Berlin, Germany). The morphology and chemical composition of the EU-biochar surface were analyzed by scanning electron microscopy (SEM), energy-dispersive X-ray (EDX), and Fourier-transform infrared (FTIR) spectroscopy.

2.2. Materials

The stock solutions (1.0 g L⁻¹) of Ni²⁺ and Pb²⁺ were prepared by dissolving 1.0 g of Ni(NO₃)₂·6H₂O (analytical grade, Tianjin Benchmark Chemical Reagent Co., Ltd., Tianjin,

China) or $\text{Pb}(\text{NO}_3)_2$ (analytical grade, Tianjin Benchmark Chemical Reagent Co.), respectively, in 1 L double distilled water. The stock solutions were further diluted with double distilled water to prepare metal solutions with known initial concentrations. Depending on the requirements of each batch experiment, the initial pH of the metal solutions was adjusted using sodium hydroxide (0.1 M) or hydrochloric acid (0.1 M).

2.3. Batch Experiments and Adsorption Performance

For the batch experiments, each metal solution (50 mL) was homogeneously mixed with the required amount of *EU*-biochar for a predetermined time in 100 mL glass funnels in a temperature and humidity controlled shaker. The samples were then filtered, and the residual metal concentration (C_t , mg L^{-1}) was measured using an ultraviolet-visible (UV-Vis) spectrophotometer, while the amount of metal uptake (q_t , mg g^{-1}) and the percentage removal (R, %) by *EU*-biochar were estimated using the following equations:

$$q_t = \frac{V}{M}(C_{in} - C_t) \quad (1)$$

$$\% \text{ Removal} = \frac{(C_{in} - C_t)}{C_{in}} \times 100 \quad (2)$$

where C_{in} (mg L^{-1}) is the initial metal concentration in the solution with volume V (L) and M (g) is the mass of *EU*-biochar. Equation (1) was also used to measure the equilibrium adsorption capacity (q_e , mg g^{-1}) against the equilibrium metal concentration (C_e ; mg L^{-1}) in the solution. Each batch test was repeated in triplicate to reduce any potential experimental error (Figures 3 and 4). The efficiency of the batch process was optimized using a contact time in the range of 1–300 min, an adsorbent dose in the range of 0.05–0.8 g, a solution pH in the range of 2.0–10.0, and an initial metal concentration in the range of 5–100 mg L^{-1} (Figures 3 and 4).

2.4. Adsorption Kinetic and Equilibrium Isotherm Models

The pseudo-first-order (PFO), pseudo-second-order (PSO), Elovich, and intraparticle diffusion of Weber and Morris (ID-WM) kinetic models and the Langmuir, Freundlich, Temkin, Halsey, Dubinin—Radushkevich (D-R), Harkins—Jura (H-J), and Jovanovic isotherm models were used in their linear and non-linear forms to elucidate the adsorption properties and adsorption mechanism of *EU*-biochar (Table 1). The values obtained for the corresponding parameters in each model using linear and non-linear regression analysis (Figures 5 and 6) are presented in Tables 2 and 3.

The adsorption data of both metal ions were analyzed using the non-linear and linear forms of four different kinetic models (Table 1), and the correlation coefficient (R^2) of each model was determined to compare their suitability in fitting the adsorption data. The parameters of the non-linear form were calculated in the OriginPro 8.5 software, while straight-line curve fitting in Microsoft Excel was used for the linear form. In order to model the adsorption data, four different initial concentrations of each metal ion with an interval of 10 mg L^{-1} were selected (Ni^{2+} : 10–40 mg L^{-1} and Pb^{2+} : 20–50 mg L^{-1}). Table 3 presents the variables calculated for each kinetic model for the selected metal ion concentrations, i.e., 20 and 40 mg L^{-1} . The *EU*-biochar dose used for the adsorption of Ni^{2+} and Pb^{2+} was kept at 0.4 and 0.2 g, respectively, while the pH of all metal solutions was maintained at 6.0 ± 0.2 .

Table 1. Linear and non-linear equations of kinetic and isotherm models.

Model	Non-Linear Form	Linear Form
<i>Kinetic</i>		
PFO	$\log(q_e - q_t) = \log q_e - \frac{k_1}{2.303} t$	$q_t = q_e(1 - \exp(-k_1 t))$
PSO	$\frac{t}{q_t} = \frac{1}{k_2 q_e^2} + \frac{1}{q_e} t$	$q_t = \frac{q_e^2 k_2 t}{q_e k_2 t + 1}$
Elovich	$q_t = \beta \ln(t) + \beta \ln(\alpha)$	$q_t = \frac{1}{\beta} \ln(1 + \alpha \beta t)$
ID-WM	$q_t = K_{ip} t^{1/2} + C$	
<i>Isotherm</i>		
Langmuir	$\frac{1}{q_e} = \frac{1}{q_m} + \left(\frac{1}{q_m K_L}\right) \frac{1}{C_e}$	$q_e = \frac{q_m K_L C_e}{(1 + K_L C_e)}$
Freundlich	$\log q_e = \log K_F + \frac{1}{n} \log C_e$	$q_e = K_F C_e^{\frac{1}{n}}$
Temkin	$q_e = \frac{RT}{b_T} \ln A_T + \frac{RT}{b_T} \ln C_e$	$q_e = \frac{RT}{H_{ads}} \ln(K_T C_e)$
Halsey	$\ln q_e = \frac{1}{n_H} \ln k_H - \frac{1}{n_H} \ln C_e$	$q_e = \exp\left(\frac{\ln k_H - \ln C_e}{n_H}\right)$
D-R	$\ln q_e = \ln q_m - K_{DR} \left(\left(RT \ln\left(1 + \frac{1}{C_e}\right)\right)^2\right)$	$q_e = q_m \exp\left(-K_{DR} \left(RT \ln\left(1 + \frac{1}{C_e}\right)\right)^2\right)$
H-J	$\frac{1}{q_e} = \left(\frac{B_{HJ}}{A_{HJ}}\right) - \left(\frac{1}{A_{HJ}}\right) \log C_e$	$q_e = \left(\frac{A_{HJ}}{B_{HJ} - \log C_e}\right)^{\frac{1}{2}}$
Jovanovic	$\ln q_e = \ln q_m - k_j C_e$	$q_e = q_m \left(1 - \exp(k_j C_e)\right)$

3. Results and Discussion

3.1. Characteristics of EU-Biochar

3.1.1. Scanning Electron Microscopy (SEM) and Energy-Dispersive X-ray (EDX) Spectroscopy Analysis

SEM analysis revealed that the outer surface of EU-biochar was rough and consisted of abundant pore structures, which may favor the adsorption of Ni²⁺ and Pb²⁺ (Figure 1a). In contrast, very small particles and some brighter zones were observed onto the adsorbent surface after the metal ion adsorption (Figure 1b,c), which could be assigned to Pb²⁺ and Ni²⁺ particles [41]. The variations in the elemental compositions of EU-biochar before and after the adsorption of Ni²⁺ and Pb²⁺ were further observed by EDX spectroscopy (Figure 1).

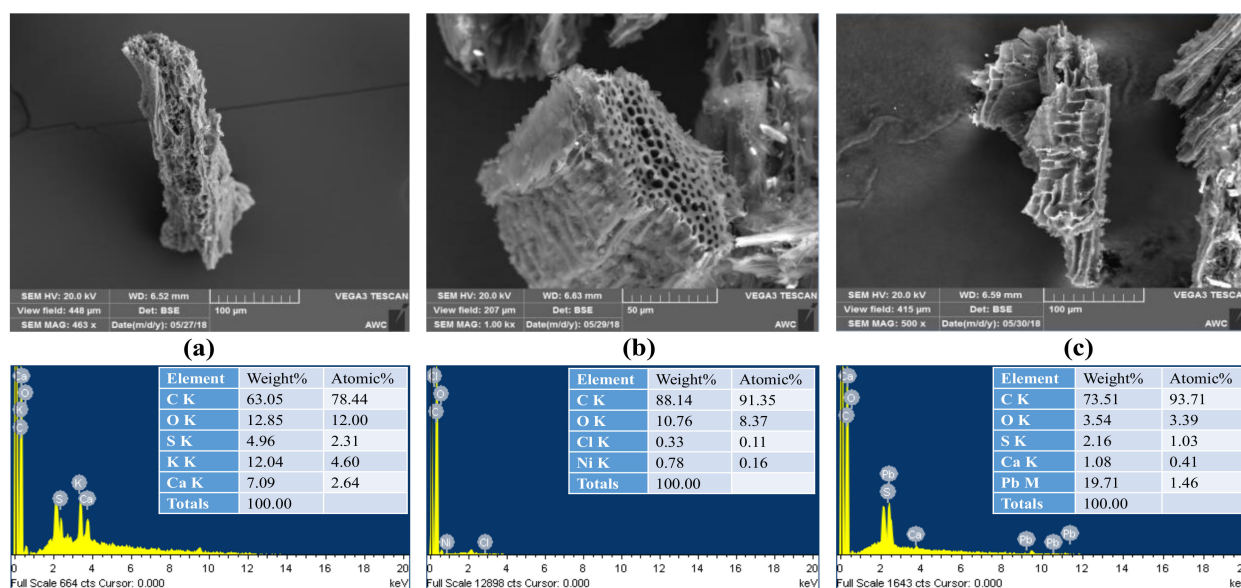


Figure 1. Scanning electron microscopy (SEM) micrographs and energy-dispersive X-ray (EDX) spectra of (a) *Eucalyptus camdulensis* (EU)-biochar, (b) Ni²⁺-loaded EU-biochar, and (c) Pb²⁺-loaded EU-biochar.

The C content of *EU*-biochar increased from 63.05% to 88.14% and 73.51% after the adsorption of Ni^{2+} and Pb^{2+} , respectively, whereas its O content decreased from 12.85% to 10.76% and 3.54%, respectively. Additionally, the adsorption of Ni^{2+} and Pb^{2+} onto the adsorbent was confirmed by the presence of 0.78% Ni^{2+} and 19.71% Pb^{2+} . These results suggested that complexes bearing C- and O-containing functional groups were generated on the biochar surface, successfully contributing to the sorption of Ni^{2+} and Pb^{2+} .

3.1.2. Fourier Transform Infrared (FTIR) Spectroscopy Analysis

The functional groups and the chemical composition of the free *EU*-biochar surface were investigated by FTIR spectroscopy. The FTIR spectra of Ni^{2+} - and Pb^{2+} -loaded *EU*-biochar were also recorded to further investigate the binding interactions between the adsorbent and the metal ions (Figure 2).

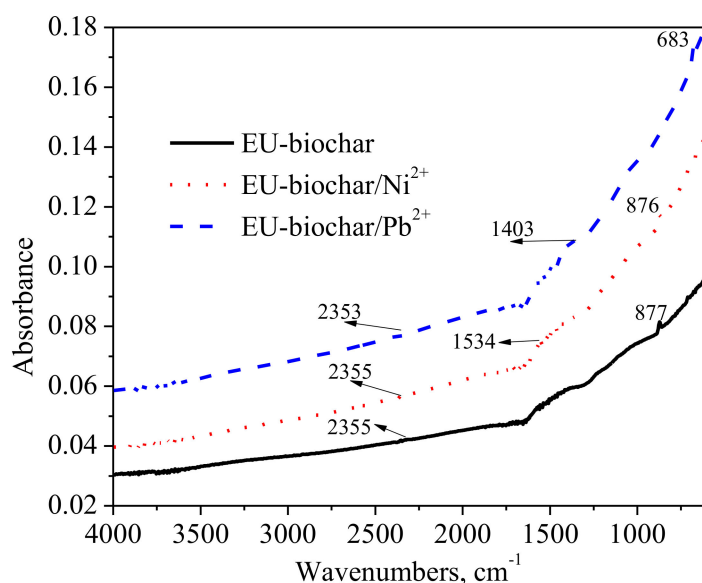


Figure 2. Fourier transform infrared (FTIR) spectra of *EU*-biochar before and after the adsorption of Ni^{2+} and Pb^{2+} .

Interestingly, no noticeable and sharp bands were observed in the recorded FTIR spectra, probably due to the high pyrolysis temperature used for the production of *EU*-biochar (600 °C). It has been previously reported that pyrolytic temperatures ≥ 500 °C can destroy most functional groups of the biochar surface due to thermalization [42]. Nevertheless, a vibrational band with very low intensity was identified at 877 cm^{-1} in the FTIR spectrum of free *EU*-biochar, which was attributed to aromatic C–H bonds. After Ni^{2+} adsorption, a slight shift from 877 to 876 cm^{-1} was observed, whereas no similar bands were detected in the spectrum of Pb^{2+} -loaded *EU*-biochar, suggesting that the surface carboxylic groups were involved in the adsorption of Ni^{2+} and Pb^{2+} . Moreover, after the adsorption of Ni^{2+} and Pb^{2+} , very weak stretching vibration bands appeared at 1534 and 1403/683 cm^{-1} , respectively, which corresponded to carboxylate and aromatic C–H groups. A weak stretching vibration peak was also detected in the spectrum of free *EU*-biochar at 2355 cm^{-1} corresponding to C=N (or CO_2 impurity), which shifted to 2353 cm^{-1} after Pb^{2+} adsorption, but remained at the same position after Ni^{2+} adsorption. Taken together, the adsorption of Ni^{2+} and Pb^{2+} onto *EU*-biochar was achieved through their complexation with the carboxylic groups of the biochar surface.

3.2. Adsorption Equilibrium and Optimization of Contact Time, Initial Metal Ion Concentrations, *EU*-Biochar Dose, and Solution pH

The changes in the uptake of both metal ions (for selected initial concentrations) and the removal efficiency of *EU*-biochar were investigated in relation to the contact

time (0–300 min) using samples with four different initial metal concentrations that were collected at regular intervals. During these experiments, the solution pH was kept constant at 6.0 and the *EU*-biochar dose for the adsorption of Ni^{2+} and Pb^{2+} was set at 0.4 and 0.2 g, respectively.

Upon immediate contact of the sample solutions with *EU*-biochar, the percentage removal and metal uptake increased rapidly due to the abundant active sites on the *EU*-biochar surface that allowed the development of numerous interactions [43], while a gradual increase was observed in both parameters as the contact time increased from 10 to 30 min (Figure 3). At this point and when the initial metal concentration was 20 mg L^{-1} , the percentage removal for Ni^{2+} and Pb^{2+} was 73% and 95%, respectively, corresponding to an adsorption capacity of 36 and 129 mg g^{-1} . However, after 30 min, the adsorption performance remained stable with insignificant ($p = 0.01$) or no changes in the percentage removal or the metal ion uptake by *EU*-biochar due to the increasing interference of solute–solute interactions. Therefore, we considered that the adsorption equilibrium was reached at 30 min. Similar changes were also observed when other initial metal concentrations were used (Figure 3). For instance, when the metal ion concentration was 40 mg L^{-1} , the percentage removal for Ni^{2+} and Pb^{2+} reached 48% and 73%, respectively, corresponding to adsorption capacities of 47 and 183 mg g^{-1} . Although the half dose of *EU*-biochar (0.2 g) was used for the adsorption of Pb^{2+} compared to Ni^{2+} (0.4 g), the percentage removal of Pb^{2+} was higher and more uptake points were identified, suggesting a faster interaction between Pb^{2+} and the biochar surface, as well as a stronger deposition of Pb^{2+} on the adsorbent surface compared to the interactions between Ni^{2+} and *EU*-biochar.

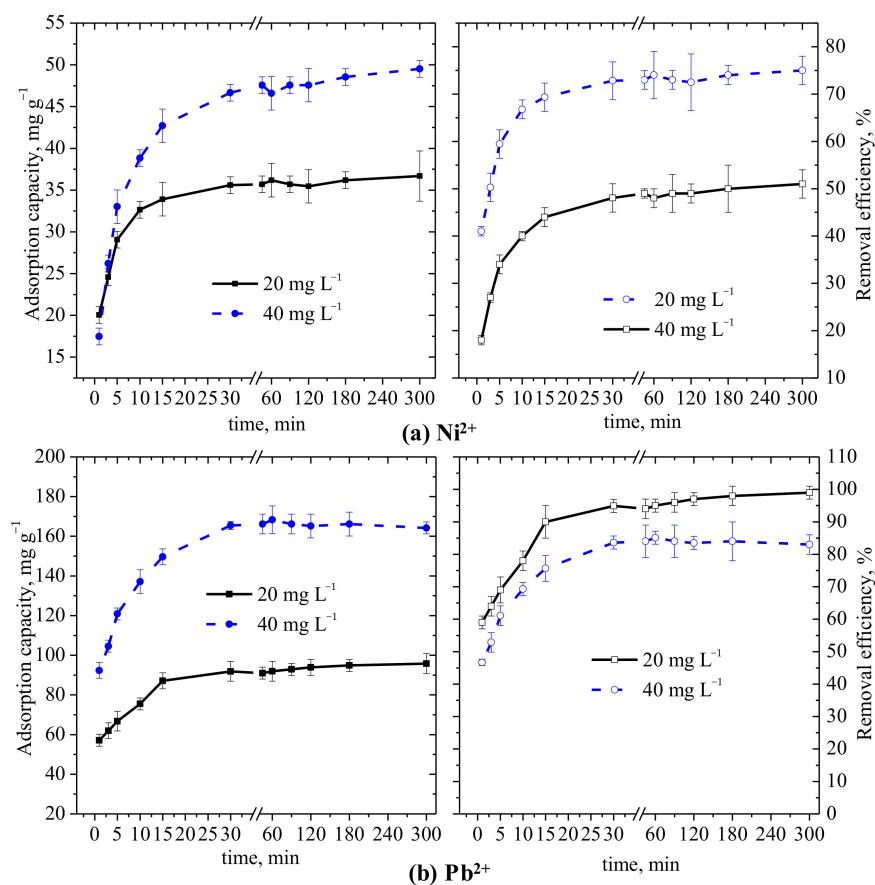


Figure 3. Optimization of the contact time with respect to the adsorption capacity and removal efficiency of *EU*-biochar for (a) Ni^{2+} and (b) Pb^{2+} .

At the adsorption equilibrium (contact time, 30 min) and a constant solution pH of 6.0, the percentage removal decreased linearly from 92% to 27% for Ni^{2+} and from 95%

to 37% for Pb^{2+} as the initial metal ion concentrations increased from 5 to 80 mg L^{-1} and from 20 to 100 mg L^{-1} , respectively (Figure 4a). This reduction could be attributed to the unavailability or saturation of the active sites of *EU*-biochar with increasing metal ion concentration and to the reduction in the ratio of fixed number of active sites to initial number of metal ions [44–47]. Moreover, the adsorption capacities showed an increasing trend with increasing initial concentrations and reached a maximum of 54 and 200 mg g^{-1} for Ni^{2+} and Pb^{2+} , respectively, at an initial concentration of 80 mg L^{-1} . This change was attributed to the increased metal ion uptake, which resulted from the high mass transfer and the reduced ionic strength of the solution at high initial concentrations. However, the uptake of metal ions started to decrease after Ni^{2+} and Pb^{2+} concentrations of 70 and 80 mg L^{-1} , respectively, suggesting that these values were the optimal concentrations for efficient adsorption performance of *EU*-biochar.

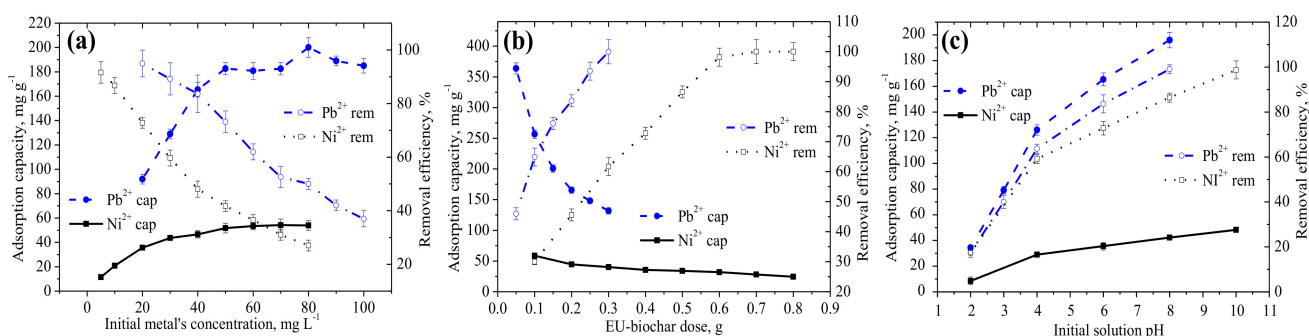


Figure 4. Optimization of (a) initial metal ion concentrations, (b) *EU*-biochar dose, and (c) initial solution pH in relation to metal ion uptake and removal efficiency of *EU*-biochar.

Due to its direct impact on the adsorption performance, the *EU*-biochar dose for the batch experiments was optimized using ranges of 0.1–0.8 g for Ni^{2+} and 0.05–0.3 g for Pb^{2+} to enhance its removal efficiency (Figure 4b). In addition, the solution pH was set at 6.0, and the initial concentrations of Ni^{2+} and Pb^{2+} were set at 20 and 40 mg L^{-1} , respectively, and the samples were shaken for 30 min. Our results indicated that, with increasing *EU*-biochar dose from 0.1 to 0.8 g, the adsorption capacity of 20 mg L^{-1} Ni^{2+} decreased by 59% (from 59 to 24 mg g^{-1}), while the percentage removal increased from 30% to 100%. In contrast, the adsorption capacity of *EU*-biochar for 40 mg L^{-1} Pb^{2+} was reduced by about 64% (from 364 to 132 mg g^{-1}) as the *EU*-biochar dose increased from 0.05 to 0.3 g, while the percentage removal increased from 46% to 100%. Therefore, 0.6 g and 0.15 g were the optimal *EU*-biochar doses to achieve the optimal percentage removal and adsorption capacity for Ni^{2+} and Pb^{2+} , respectively. We also reasoned that a high amount of *EU*-biochar would provide a larger surface area and a higher number of active sites for the selected metal ion concentrations, resulting in less significant changes in the percentage removal.

A pH range of 2.0–10.0 and 2.0–8.0 was also selected to determine its effect on the adsorption performance after mixing 20 and 40 mg L^{-1} Ni^{2+} and Pb^{2+} with 0.4 and 0.2 g *EU*-biochar, respectively, for 30 min. In particular, as the pH of the Ni^{2+} solution increased from 2.0 to 10.0, the adsorption capacity of *EU*-biochar for Ni^{2+} increased from 9 to 48 mg g^{-1} and the percentage removal increased from 17% to 99% (Figure 4c). The low initial adsorption capacity and percentage removal were attributed to the excess amount of positively charged H^+ (at low pH values), which competed with the positively charged metal ions for adsorption on the negatively charged biochar surface [48,49]. Similarly, the adsorption capacity of *EU*-biochar for Pb^{2+} increased from 34 to 196 mg g^{-1} with increasing pH, while the percentage removal showed the same trend as that of Ni^{2+} due to the improved electrostatic interactions between the negatively charged biochar surface at high pH values and the positively charged Pb^{2+} (Figure 4c) [49–51]. A comparison of the

adsorption capacities of *EU*-biochar with that of other adsorbents for the studied metal ions is presented in Table 2.

Table 2. Performance comparison of *EU*-biochar with other previously reported biochar used for the removal of Pb^{2+} and Ni^{2+} ions.

Biomass	Pyrolysis Temp (°C)	Holding Time	Pollutants	Q _{max} (mg g ⁻¹)	Isotherm	Kinetic Models	Reference
<i>EU</i> -biochar	600	6 h	Ni^{2+}	54	Langmuir	PSO	This work
<i>EU</i> -biochar	600	6 h	Pb^{2+}	200	Langmuir	PSO	This work
Rice husk biochar	300	20 min	Pb^{2+}	1.84	Langmuir	PSO	[52]
Pine wood biochar	300	20 min	Pb^{2+}	3.89	Langmuir	PSO	[52]
Hickory wood biochar	600	2 h	Pb^{2+}	11.2	Langmuir	PSO	[31]
Date seed biochar	550	3 h	Pb^{2+}	74.60	Freundlich, Langmuir	PSO	[53]
Buffalo weed biochar	700	4 h	Pb^{2+}	333.3	Langmuir	PSO	[54]
Corn cob biochar	600	2 h	Ni^{2+}	15.40	Langmuir	Elovich model	[55]
Sugar cane bagasse biochar	600	2 h	Ni^{2+}	38.15	Redlich-Peterson	PFO	[56]

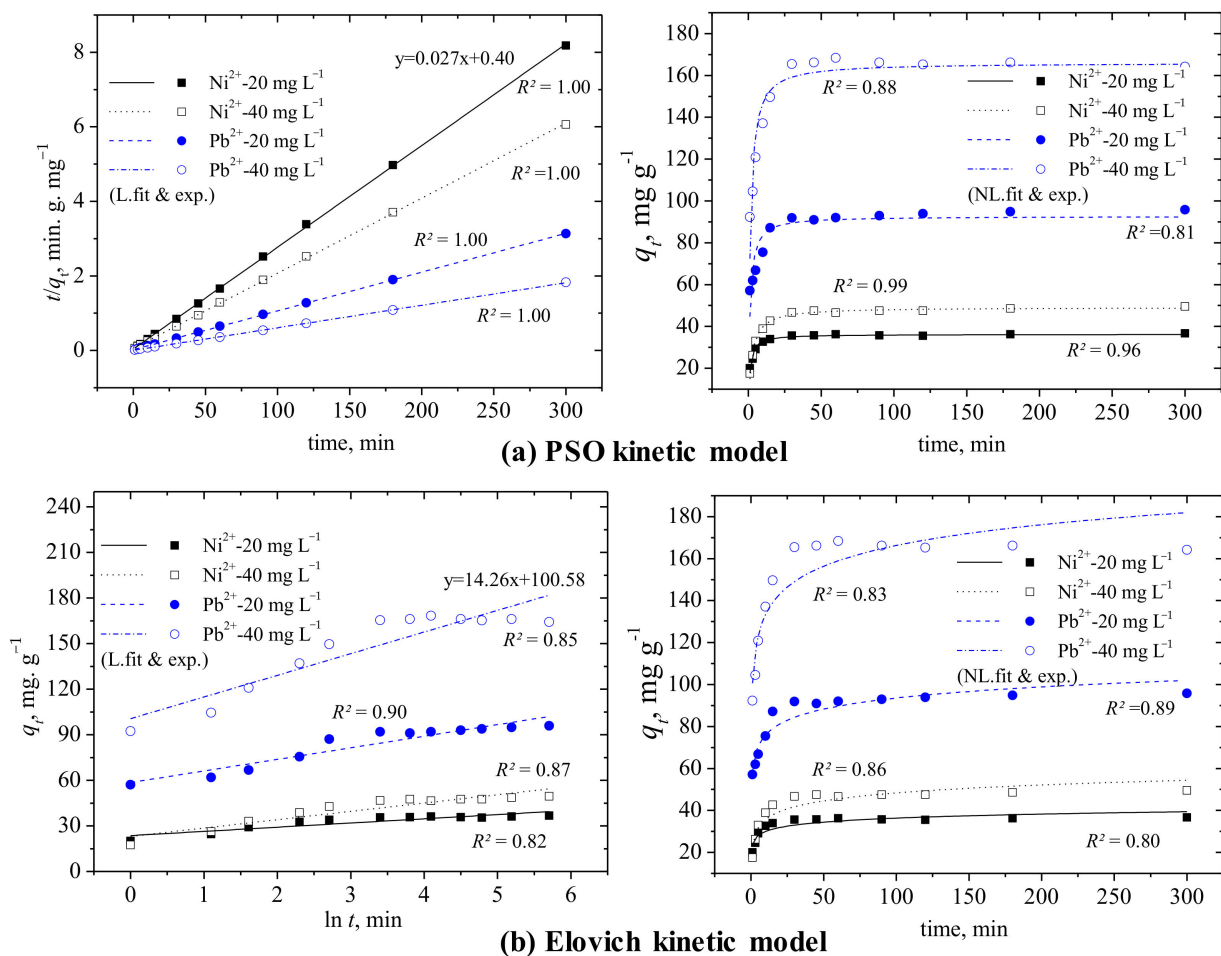
3.3. Evaluation of the Adsorption Data through Kinetic Fitting Models

Very low R^2 values (0.2–0.36) in the linearized PFO kinetic model reflected a poor fitting of the model to the adsorption data of both metal ions, confirming its applicability only for the initial stage (contact time) of adsorption [57,58]. The non-linear form of the PFO model showed a better fitting to the adsorption of Ni^{2+} than that of Pb^{2+} , especially at high initial concentrations (30 and 40 mg L⁻¹). Moreover, the estimated adsorption capacities ($q_{e \text{ cal}}$) were considerably lower than the experimental values in the linear PFO model, whereas the $q_{e \text{ cal}}$ values in the non-linear form were slightly lower than the experimental values except for the adsorption of Pb^{2+} at 40 mg L⁻¹. In addition, the rate constant k_1 was significantly lower in the linear than in the non-linear form of the PFO model with the Pb^{2+} adsorption showing higher values than Ni^{2+} (Table 3).

The adsorption data of all tested Ni^{2+} and Pb^{2+} concentrations were perfectly fitted to the linear form of the PSO kinetic model with R^2 values of ~1.0 (Figure 5a). Similar results were obtained for the adsorption of Ni^{2+} ($R^2 = 0.94\text{--}0.99$) using the non-linear form of the PSO model, while the adsorption data of Pb^{2+} were good fitted ($R^2 = 0.81\text{--}0.88$), confirming the chemisorption of both metal ions onto *EU*-biochar, consistent with previous studies [59–61]. The rate constant k_2 in the PSO kinetic model decreased with increasing initial concentrations of both metal ions, but a reverse trend was observed for the linearized fitting to the adsorption data of Pb^{2+} . However, the correlation of the initial adsorption rate (h) with the initial metal ion concentrations could not be predicted easily. In particular, the h value was higher for 20 mg L⁻¹ Ni^{2+} than for 40 mg L⁻¹ Ni^{2+} , but an opposite trend was observed for Pb^{2+} using both forms of the PSO kinetic model (Table 3). Moreover, the $q_{e \text{ cal}}$ value was closer to the experimental value only in the non-linear PSO model, but deviated from the experimental value by about 7% for 40 mg L⁻¹ Pb^{2+} in both model forms.

Table 3. Calculated variables in the linear and non-linear forms of the kinetic models used to model the adsorption of 20 and 40 mg L⁻¹ Ni²⁺ and Pb²⁺ onto EU-biochar.

Kinetic Model	Parameter	Linear Form				Non-Linear Form			
		Ni ²⁺ (mg L ⁻¹)		Pb ²⁺ (mg L ⁻¹)		Ni ²⁺ (mg L ⁻¹)		Pb ²⁺ (mg L ⁻¹)	
		20	40	20	40	20	40	20	40
	$q_{e \text{ exp}}$ (mg g ⁻¹)	36.19	46.60	91.95	179.61	36.19	46.60	91.95	179.61
PFO	$q_{e \text{ cal}}$ (mg g ⁻¹)	2.90	5.39	5.27	34.15	34.98	46.79	89	159.84
	k_1 (min ⁻¹)	0.007	0.009	0.009	0.005	0.53	0.26	0.54	0.43
	R^2	0.24	0.36	0.2	0.32	0.76	0.92	0.46	0.64
PSO	$q_{e \text{ cal}}$ (mg g ⁻¹)	36.63	49.75	96.15	166.67	36.23	49.1	92.67	166.05
	k_2 (g mg ⁻¹ min ⁻¹)	0.019	0.007	0.0049	0.0082	0.027	0.009	0.0100	0.0047
	h (mg g ⁻¹ min ⁻¹)	24.88	17.39	45.66	227.27	34.98	21.24	86.22	128.21
	R^2	0.9999	0.9998	0.9999	0.9998	0.96	0.99	0.81	0.88
Elovich	α (mg g ⁻¹ min ⁻¹)	5151.96	67.51	2160.36	1154.38	14,247.5	374.38	16,459.4	16,489
	β (g mg ⁻¹)	2.76	5.48	7.62	14.26	0.36	0.18	0.13	0.07
	R^2	0.82	0.87	0.9	0.85	0.8	0.86	0.89	0.83
ID-WM	K_{ip} (mg g ⁻¹ min ^{1/2})	0.75	1.53	2.21	3.91	0.75	1.53	2.21	3.9
	C (mg g ⁻¹)	27.48	30.46	68.08	120.09	27.48	30.46	68.1	120.1
	R^2	0.5	0.57	0.63	0.54	0.5	0.57	0.63	0.54

**Figure 5.** Examples of the linearized and non-linear fitting of the (a) PSO and (b) Elovich kinetic models to the adsorption data of Ni²⁺ and Pb²⁺ at 20 and 40 mg L⁻¹.

Both the linear and non-linear forms of the Elovich kinetic model yielded good R^2 values (0.80–0.90) for all tested initial concentrations of Ni^{2+} and Pb^{2+} , suggesting that both metal ions were adsorbed via activated chemical adsorption without desorption (Figure 5b) [43]. However, in most cases, the relationship of the initial adsorption rate constant (α) with the initial concentrations could not be established by estimating its highest values at low initial concentrations. Moreover, based on the calculated β values in linearized fitting, the number of sites available for adsorption [62] and the activation energy of chemisorption [63] increased with increasing initial metal ion concentrations, whereas non-linear fitting showed an opposite trend corresponding to the decreasing β values (Table 3).

Furthermore, the ID–WM kinetic model yielded high values of parameter C , an indicator of the boundary layer thickness, suggesting a greater boundary layer effect on the adsorption process at high initial metal ion concentrations. The model rate constant K_{ip} also increased as the initial metal ion concentrations increased in both model forms. However, the R^2 values ranged between 0.50–0.63 (Table 3) and did not allow the prediction of multilayer adsorption of Ni^{2+} and Pb^{2+} onto *EU*-biochar.

3.4. Evaluation of the Adsorption Data through Isotherm Fitting Models

Several two-parameter isotherm models were also applied to the adsorption data of Ni^{2+} and Pb^{2+} (Table 1), and the adsorption performance of Ni^{2+} (5–80 mg L^{-1}) and Pb^{2+} (20–100 mg L^{-1}) onto 0.4 and 0.2 g *EU*-biochar, respectively, at a solution pH of 6.0 ± 0.2 was assessed using both the linearized and non-linear forms of the models (Table 4). The regressions of the linear and non-linear forms of isotherms were solved using the OriginPro 8.5 and Curve Expert Professional software, respectively. Based on the experimental data, the maximum adsorption capacities were achieved when the initial concentrations of Ni^{2+} and Pb^{2+} were 80 and 100 mg L^{-1} , respectively. Therefore, the maximum adsorption capacities at 80 mg L^{-1} were selected to compare the theoretical calculated values of both metal ions in each model.

The Langmuir model proved to be promising in explaining the monolayer adsorption of both metal ions due to the high R^2 values (0.96–0.99) and nearly perfect fitting using both regression forms (Figure 6a). The estimated maximum adsorption capacity of the model (q_m) was close to the experimental values for both metal ions (54 mg g^{-1} for Ni^{2+} and 200 mg g^{-1} for Pb^{2+}) with a slightly better agreement of the non-linear form (Table 4). Lower values of the Langmuir constant (K_L) were also found in the non-linear form for both metal ions (Table 4), while K_L was almost double for Pb^{2+} (0.81 L mg^{-1}) than for Ni^{2+} (0.41 L mg^{-1}), implying a higher affinity of Pb^{2+} for *EU*-biochar compared to Ni^{2+} . In addition, the dimensionless separation factor, $R_L [(1 + K_L C_0)^{-1}]$, had almost the same value for both the linearized and non-linear Langmuir model, suggesting a similar isotherm shape for both model forms [64]. This similarity was, however, not observed for the adsorption of Ni^{2+} onto *EU*-biochar.

The q_m values of the non-linear and linear Freundlich isotherm model were by 4% and 8% higher than the experimental values for the adsorption of Pb^{2+} , respectively, while an overestimation of 17% and 10% was observed for Ni^{2+} (Table 4). However, the adsorption data of Ni^{2+} were well fitted to the model with R^2 values ranging between 0.94–0.95 (Figure 6b), while a reasonable fit to the data of Pb^{2+} was also achieved with R^2 of 0.85 and 0.81 for the linear and non-linear form, respectively. The suitability of the model was further confirmed by the dimensionless factor (n), which was >1.0 for both metal ions, suggesting the surface heterogeneity of *EU*-biochar ($1/n = 0–1.0$) [65]. Moreover, the model constant K_F was higher in the non-linear form for both metal ions, but deviated significantly from the favorable range [1–20 (mg g^{-1}) (L mg^{-1}) $^{1/n}$], except for the adsorption of Ni^{2+} in the linear form (Table 4), suggesting that the Freundlich isotherm model could not be used to predict metal ion adsorption.

Table 4. Calculated values of the variables in the linear and non-linear forms of the isotherm models used to model the adsorption of Ni²⁺ and Pb²⁺ (80 mg L⁻¹) onto EU-biochar.

Isotherm Model	Parameter	Ni ²⁺		Pb ²⁺	
		Linear	Non-Linear	Linear	Non-Linear
	$q_{e \text{ exp}}, \text{ mg g}^{-1}$		54		200
Langmuir	$q_m, \text{ mg g}^{-1}$	50.51	55.21	192.31	193.95
	$K_L, \text{ L mg}^{-1}$	0.68	0.41	0.91	0.81
	R_L	0.018	0.029	0.014	0.015
	R^2	0.99	0.98	0.98	0.96
Freundlich	$q_m, \text{ mg g}^{-1}$	59.46	63.35	215.02	207.79
	$K_F, (\text{mg g}^{-1}) (\text{L mg}^{-1})^{1/n}$	15.54	21.48	106.28	114.00
	$1/n$	0.306	0.247	0.161	0.137
	R^2	0.95	0.94	0.85	0.81
Temkin	$K_T, \text{ L mg}^{-1}$	8.70	8.70	106.16	106.15
	$H_{ads}, \text{ kJ mol}^{-1}$	277.50	277.5	110.75	110.75
	R^2	0.99	0.99	0.88	0.87
Halsey	$q_{e \text{ cal}}, \text{ mg g}^{-1}$	61.01	58.78	245.36	195.00
	n_H	-3.27	-4.05	-6.22	-7.30
	K_H	0.323	0.000	0.264	0.000
	R^2	0.95	0.94	0.85	0.81
D-R	$q_m, \text{ mg g}^{-1}$	45.95	49.31	179.68	181.64
	$K_{DR}, (\text{mol kJ}^{-1})^2$	2.0×10^{-7}	4.0×10^{-7}	2.0×10^{-7}	2.6×10^{-7}
	$E, \text{ kJ mol}^{-1}$	1.58	1.12	1.58	1.39
H-J	R^2	0.85	0.82	0.86	0.81
	$A_{HJ}, \text{ mg g}^{-1}$	357.14	147.39	25000	1076.7
	B_{HJ}	1.5357	3	2.25	4.47
Jovanovic	R^2	0.72	0.86	0.76	0.76
	$q_m, \text{ mg g}^{-1}$	23.89	50.9	134.05	184.39
	$K_j, \text{ L g}^{-1}$	-0.019	-0.28	-0.007	-0.49
	R^2	0.55	0.91	0.46	0.87

Compared to the Freundlich isotherm model, the Temkin model provided a better fit to the adsorption data of both metal ions with a perfect fit to the adsorption of Ni²⁺ ($R^2 = 0.99$), reflecting the heterogeneous adsorption of Ni²⁺ onto EU-biochar with uniform distribution of binding energies [66]. In addition, a considerably lower binding constant at equilibrium (K_T) and a higher heat of adsorption (H_{ads}) were observed for the adsorption of Ni²⁺ compared to the adsorption of Pb²⁺ (Table 4).

The Halsey model yielded exactly the same R^2 values as the Freundlich model with higher R^2 for the adsorption of Ni²⁺ than Pb²⁺ and slightly better results in the linear than the non-linear form. The $q_{e \text{ cal}}$ values of the non-linear form were closer to the experimental values compared to the linear form. In addition, the model constant and exponent (K_H and n_H , respectively) were higher for the adsorption of Ni²⁺ than for the adsorption of Pb²⁺, while the linearized fitting yielded higher K_H values than the non-linear fitting ($K_H = 0$) for both metal ions (Table 4).

The D-R isotherm provided good R^2 values (0.81–0.86) for both metal ions, while linear fitting yielded slightly higher R^2 values than the non-linear fitting. However, the theoretical $q_{e \text{ cal}}$ of the non-linear form agreed more with the experimental values compared to that of the linear form for both metal ions (Table 4). Considering also the calculated values of the mean free energy of adsorption [$E = (2K_{DR})^{-1/2}$, $<8 \text{ kJ mol}^{-1}$] resulting from the significantly low values of the model constant ($K_{DR} \sim 0$, Table 4), the D-R model suggested that both metal ions were physisorbed onto EU-biochar.

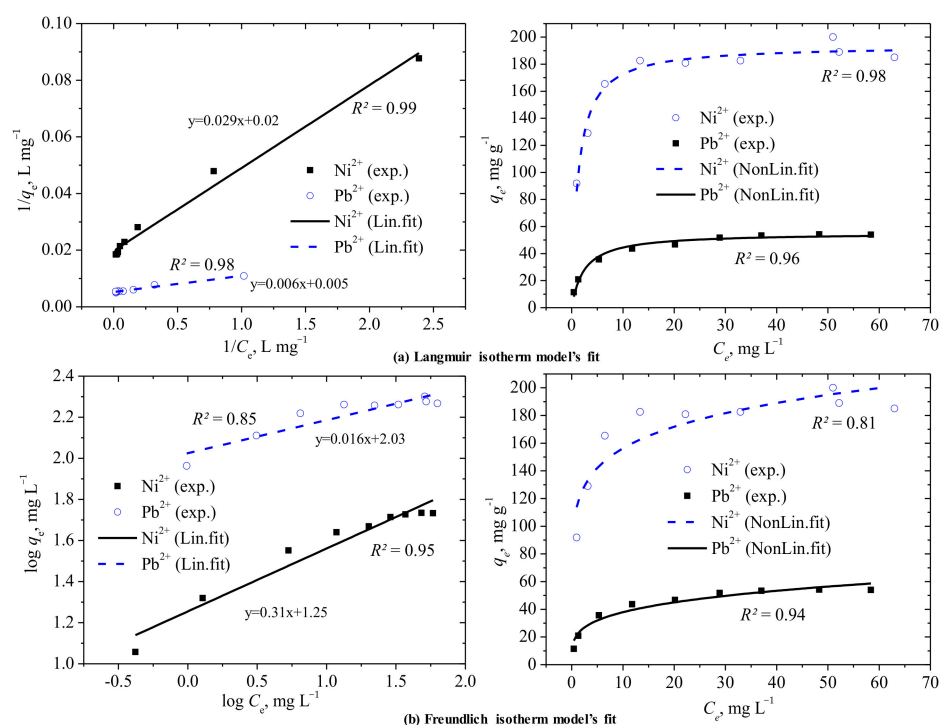


Figure 6. Examples of the non-linear and linear fitting of the (a) Langmuir and (b) Freundlich isotherm models to the adsorption data of Ni^{2+} and Pb^{2+} at 20 and 40 mg L^{-1} .

A reasonable fit to the adsorption data of Ni^{2+} was also estimated by the non-linear H–J isotherm with $R^2 = 0.86$ (Table 4), supporting its multilayer adsorption onto *EU*-biochar with heterogeneous pore distribution, similar to the Freundlich and Halsey models. The model constant A_{HJ} was much higher in the linear than in the non-linear form for both metal ions, while A_{HJ} and B_{HJ} (model constant) were significantly higher for the adsorption of Pb^{2+} than for the adsorption of Ni^{2+} . In addition, the B_{HJ} values in the non-linear H–J isotherm were almost double the values in the linear isotherm for both metal ions.

The linear form of the Jovanovic isotherm was not satisfactory due to the very low R^2 values (0.55 and 0.46 for Ni^{2+} and Pb^{2+} , respectively) and the great deviation of the theoretical from the experimental q_m values. The model constant K_j was higher for the adsorption of Ni^{2+} than for the adsorption of Pb^{2+} in the linear form of the model, while a reverse trend was observed in the non-linear form (Table 4). In addition, the non-linear Jovanovic model provided satisfactory results with R^2 values of 0.91 and 0.87 and slightly underestimated theoretical q_m values of about 6% and 8% compared to the experimental values for Ni^{2+} and Pb^{2+} , respectively. Thus, similar to the Langmuir model, the non-linear Jovanovic model supported the localized monolayer adsorption of both metal ions onto *EU*-biochar without lateral interactions, suggesting the development of mechanical interactions between the adsorbed and desorbed molecules [67,68].

4. Conclusions

EU-biochar produced via thermal degradation from *EU* sawdust was used as a potential adsorbent for Ni^{2+} and Pb^{2+} contaminants in synthetic wastewater. EDX and FTIR spectroscopy demonstrated that the metal ions were successfully adsorbed by interacting with the carboxylic groups on the biochar surface. Further experiments on the uptake of both metal ions and the removal efficiency of *EU*-biochar indicated that the adsorption equilibrium was reached at 30 min, while Pb^{2+} was removed faster than Ni^{2+} , suggesting the development of stronger and faster interactions between Pb^{2+} and the *EU*-biochar surface. Additional studies by varying the initial metal ion concentration, the adsorbent dose, and the pH of the metal solutions indicated that the simultaneous improvement of

the adsorption capacity of *EU*-biochar and the corresponding percentage removal for Ni^{2+} and Pb^{2+} could only be achieved by increasing the pH of the metal solutions from 2.0 to 10.0 and from 2.0 to 8.0, respectively.

A series of kinetic and isotherm fitting models were further employed to study the removal mechanism of Ni^{2+} and Pb^{2+} . The adsorption data fitted well to the linear and non-linear forms of the PSO and Elovich kinetic models, suggesting activated chemisorption as the removal mechanism of both metal ions. Among the applied isotherm models, the Langmuir model could adequately explain the monolayer adsorption of both metal ions, while the Temkin model fitted perfectly the adsorption data of Ni^{2+} , suggesting its heterogeneous adsorption onto *EU*-biochar. The non-linear D–R isotherm also suggested that both metal ions are adsorbed onto *EU*-biochar via physisorption, while the non-linear H–J isotherm supported the multilayer adsorption of Ni^{2+} with heterogeneous pore distribution. Finally, the non-linear Jovanovic model supported the localized monolayer adsorption of both metal ions onto *EU*-biochar without lateral interactions.

Author Contributions: Conceptualization, M.T.A. and M.S.; methodology, M.S.; software, M.T.A. and A.A.A.; validation, M.T.A. and M.S.; formal analysis, M.S.; investigation, M.T.A. and A.A.A.; resources, A.A.A.; data curation, M.T.A. and M.S.; writing—original draft preparation, M.T.A.; writing—review and editing, M.T.A. and M.S.; visualization, M.S.; supervision, M.T.A.; project administration, A.A.A. and M.S.; funding acquisition, A.A.A. All authors have read and agreed to the published version of the manuscript.

Funding: This project was funded by the National Plan for Science, Technology and Innovation (MAARIFAH), King Abdulaziz City for Science and Technology, Kingdom of Saudi Arabia, Award Number (12-WAT2623-02).

Acknowledgments: The authors appreciate the Deanship of Scientific Research and RSSU at King Saud University for their technical support (manuscript editing services).

Conflicts of Interest: The authors declare no conflict of interest.

References

- Zhang, P.; Yang, D.; Zhang, Y.; Li, Y.; Liu, Y.; Cen, Y.; Zhang, W.; Geng, W.; Rong, T.; Liu, Y.; et al. Re-Examining the Drive Forces of China's Industrial Wastewater Pollution Based on GWR Model at Provincial Level. *J. Clean. Prod.* **2020**, *262*, 121309. [[CrossRef](#)]
- Shafiq, M.; Alazba, A.A.; Amin, M.T. Removal of Heavy Metals from Wastewater Using Date Palm as a Biosorbent: A Comparative Review. *Sains Malays.* **2018**, *47*, 35–49. [[CrossRef](#)]
- Saritas, O.; Proskuryakova, L.N. Water Resources—an Analysis of Trends, Weak Signals and Wild Cards with Implications for Russia. *Foresight* **2017**, *19*, 152–173. [[CrossRef](#)]
- Qi, M.; Yang, Y.; Zhang, X.; Zhang, X.; Wang, M.; Zhang, W.; Lu, X.; Tong, Y. Pollution Reduction and Operating Cost Analysis of Municipal Wastewater Treatment in China and Implication for Future Wastewater Management. *J. Clean. Prod.* **2020**, *253*, 120003. [[CrossRef](#)]
- Mohan, D.; Sarswat, A.; Ok, Y.S.; Pittman, C.U. Organic and Inorganic Contaminants Removal from Water with Biochar, a Renewable, Low Cost and Sustainable Adsorbent—A Critical Review. *Bioresour. Technol.* **2014**, *160*, 191–202. [[CrossRef](#)]
- Islam, M.A.; Awual, M.R.; Angove, M.J. A Review on Nickel(II) Adsorption in Single and Binary Component Systems and Future Path. *J. Environ. Chem. Eng.* **2019**, *7*, 103–305. [[CrossRef](#)]
- Hua, M.; Zhang, S.; Pan, B.; Zhang, W.; Lv, L.; Zhang, Q. Heavy Metal Removal from Water/Wastewater by Nanosized Metal Oxides: A Review. *J. Hazard. Mater.* **2012**, *211–212*, 317–331. [[CrossRef](#)]
- Cerná, M. Use of Solvent Extraction for the Removal of Heavy Metals from Liquid Wastes. *Environ. Monit. Assess.* **1995**, *34*, 151–162. [[CrossRef](#)] [[PubMed](#)]
- Bashir, A.; Malik, L.A.; Ahad, S.; Manzoor, T.; Bhat, M.A.; Dar, G.N.; Pandith, A.H. Removal of Heavy Metal Ions from Aqueous System by Ion-Exchange and Biosorption Methods. *Environ. Chem. Lett.* **2019**, *17*, 729–754. [[CrossRef](#)]
- Barakat, M.A. New Trends in Removing Heavy Metals from Industrial Wastewater. *Arab. J. Chem.* **2011**, *4*, 361–377. [[CrossRef](#)]
- Oncel, M.S.; Muhcu, A.; Demirbas, E.; Kobya, M. A Comparative Study of Chemical Precipitation and Electrocoagulation for Treatment of Coal Acid Drainage Wastewater. *J. Environ. Chem. Eng.* **2013**, *1*, 989–995. [[CrossRef](#)]
- Ahmad, J.; Naeem, S.; Ahmad, M.; Usman, A.R.A.; Al-Wabel, M.I. A Critical Review on Organic Micropollutants Contamination in Wastewater and Removal through Carbon Nanotubes. *J. Environ. Manag.* **2019**, *246*, 214–228. [[CrossRef](#)] [[PubMed](#)]
- Wang, X.S.; Miao, H.H.; He, W.; Shen, H.L. Competitive Adsorption of Pb(II), Cu(II), and Cd(II) Ions on Wheat-Residue Derived Black Carbon. *J. Chem. Eng. Data* **2011**, *56*, 444–449. [[CrossRef](#)]

14. Yu, J.-X.; Wang, L.-Y.; Chi, R.-A.; Zhang, Y.-F.; Xu, Z.-G.; Guo, J. Competitive Adsorption of Pb²⁺ and Cd²⁺ on Magnetic Modified Sugarcane Bagasse Prepared by Two Simple Steps. *Appl. Surf. Sci.* **2013**, *268*, 163–170. [[CrossRef](#)]
15. Reddy, N.; Yang, Y. Biofibers from Agricultural Byproducts for Industrial Applications. *Trends Biotechnol.* **2005**, *23*, 22–27. [[CrossRef](#)] [[PubMed](#)]
16. Oh, T.K.; Choi, B.; Shinogi, Y.; Chikushi, J. Characterization of Biochar Derived from Three Types of Biomass. *J. Fac. Agric. Kyushu Univ.* **2012**, *57*, 61–66. [[CrossRef](#)]
17. Sciban, M.; Radetic, B.; Kevresan, Z.; Klasnja, M. Adsorption of Heavy Metals from Electroplating Wastewater by Wood Sawdust. *Bioresour. Technol.* **2007**, *98*, 402–409. [[CrossRef](#)]
18. Sud, D.; Mahajan, G.; Kaur, M. Agricultural Waste Material as Potential Adsorbent for Sequestering Heavy Metal Ions from Aqueous Solutions—A Review. *Bioresour. Technol.* **2008**, *99*, 6017–6027. [[CrossRef](#)]
19. Muramatsu, H.; Kim, Y.A.; Yang, K.-S.; Cruz-Silva, R.; Toda, I.; Yamada, T.; Terrones, M.; Endo, M.; Hayashi, T.; Saitoh, H. Rice Husk-Derived Graphene with Nano-Sized Domains and Clean Edges. *Small* **2014**, *10*, 2766–2770. [[CrossRef](#)]
20. Suman; Kardam, A.; Gera, M.; Jain, V.K. A Novel Reusable Nanocomposite for Complete Removal of Dyes, Heavy Metals and Microbial Load from Water Based on Nanocellulose and Silver Nano-Embedded Pebbles. *Environ. Technol.* **2015**, *36*, 706–714. [[CrossRef](#)]
21. Inyang, M.; Gao, B.; Yao, Y.; Xue, Y.; Zimmerman, A.; Mosa, A.; Pullammanappallil, P.; Ok, Y.S.; Cao, X. A Review of Biochar as a Low-Cost Adsorbent for Aqueous Heavy Metal Removal. *Crit. Rev. Environ. Sci. Technol.* **2016**, *46*, 406–433. [[CrossRef](#)]
22. Huang, G.; Wang, D.; Ma, S.; Chen, J.; Jiang, L.; Wang, P. A New, Low-Cost Adsorbent: Preparation, Characterization, and Adsorption Behavior of Pb(II) and Cu(II). *J. Colloid Interface Sci.* **2015**, *445*, 294–302. [[CrossRef](#)]
23. Xie, Y.; Yuan, X.; Wu, Z.; Zeng, G.; Jiang, L.; Peng, X.; Li, H. Adsorption Behavior and Mechanism of Mg/Fe Layered Double Hydroxide with Fe₃O₄-Carbon Spheres on the Removal of Pb(II) and Cu(II). *J. Colloid Interface Sci.* **2019**, *536*, 440–455. [[CrossRef](#)]
24. Bouhamed, F.; Elouear, Z.; Bouzid, J.; Ouddane, B. Batch Sorption of Pb(II) Ions from Aqueous Solutions Using Activated Carbon Prepared from Date Stones: Equilibrium, Kinetic, and Thermodynamic Studies. *Desalination Water Treat.* **2014**, *52*, 2261–2271. [[CrossRef](#)]
25. Yang, R.; Li, H.; Huang, M.; Yang, H.; Li, A. A Review on Chitosan-Based Flocculants and Their Applications in Water Treatment. *Water Res.* **2016**, *95*, 59–89. [[CrossRef](#)]
26. Hegazi, H.A. Removal of Heavy Metals from Wastewater Using Agricultural and Industrial Wastes as Adsorbents. *HBRC J.* **2013**, *9*, 276–282. [[CrossRef](#)]
27. Sočo, E.; Kalemekiewicz, J. Adsorption of Nickel(II) and Copper(II) Ions from Aqueous Solution by Coal Fly Ash. *J. Environ. Chem. Eng.* **2013**, *1*, 581–588. [[CrossRef](#)]
28. Song, M.; Wei, Y.; Cai, S.; Yu, L.; Zhong, Z.; Jin, B. Study on Adsorption Properties and Mechanism of Pb²⁺ with Different Carbon Based Adsorbents. *Sci. Total Environ.* **2018**, *618*, 1416–1422. [[CrossRef](#)] [[PubMed](#)]
29. Jindo, K.; Mizumoto, H.; Sawada, Y.; Sanchez-Monedero, M.A.; Sonoki, T. Physical and Chemical Characterization of Biochars Derived from Different Agricultural Residues. *Biogeosciences* **2014**, *11*, 6613–6621. [[CrossRef](#)]
30. Zhao, J.; Shen, X.-J.; Domene, X.; Alcañiz, J.-M.; Liao, X.; Palet, C. Comparison of Biochars Derived from Different Types of Feedstock and Their Potential for Heavy Metal Removal in Multiple-Metal Solutions. *Sci. Rep.* **2019**, *9*, 9869. [[CrossRef](#)]
31. Ding, Z.; Hu, X.; Wan, Y.; Wang, S.; Gao, B. Removal of Lead, Copper, Cadmium, Zinc, and Nickel from Aqueous Solutions by Alkali-Modified Biochar: Batch and Column Tests. *J. Ind. Eng. Chem.* **2016**, *33*, 239–245. [[CrossRef](#)]
32. Ahmad, M.; Ahmad, M.; Usman, A.R.A.; Al-Faraj, A.S.; Ok, Y.S.; Hussain, Q.; Abduljabbar, A.S.; Al-Wabel, M.I. An Efficient Phosphorus Scavenging from Aqueous Solution Using Magnesiothermally Modified Bio-Calcite. *Environ. Technol.* **2017**, 1–12. [[CrossRef](#)]
33. Wang, L.; Wang, Y.; Ma, F.; Tankpa, V.; Bai, S.; Guo, X.; Wang, X. Mechanisms and Reutilization of Modified Biochar Used for Removal of Heavy Metals from Wastewater: A Review. *Sci. Total Environ.* **2019**, *668*, 1298–1309. [[CrossRef](#)]
34. Ahmad, M.; Rajapaksha, A.U.; Lim, J.E.; Zhang, M.; Bolan, N.; Mohan, D.; Vithanage, M.; Lee, S.S.; Ok, Y.S. Biochar as a Sorbent for Contaminant Management in Soil and Water: A Review. *Chemosphere* **2014**, *99*, 19–33. [[CrossRef](#)]
35. Li, H.; Dong, X.; da Silva, E.B.; de Oliveira, L.M.; Chen, Y.; Ma, L.Q. Mechanisms of Metal Sorption by Biochars: Biochar Characteristics and Modifications. *Chemosphere* **2017**, *178*, 466–478. [[CrossRef](#)]
36. Xu, X.; Cao, X.; Zhao, L. Comparison of Rice Husk- and Dairy Manure-Derived Biochars for Simultaneously Removing Heavy Metals from Aqueous Solutions: Role of Mineral Components in Biochars. *Chemosphere* **2013**, *92*, 955–961. [[CrossRef](#)]
37. Kloss, S.; Zehetner, F.; Dellantonio, A.; Hamid, R.; Ottner, F.; Liedtke, V.; Schwanninger, M.; Gerzabek, M.H.; Soja, G. Characterization of Slow Pyrolysis Biochars: Effects of Feedstocks and Pyrolysis Temperature on Biochar Properties. *J. Environ. Qual.* **2012**, *41*, 990–1000. [[CrossRef](#)]
38. Suliman, W.; Harsh, J.B.; Abu-Lail, N.I.; Fortuna, A.-M.; Dallmeyer, I.; Garcia-Perez, M. Influence of Feedstock Source and Pyrolysis Temperature on Biochar Bulk and Surface Properties. *Biomass Bioenergy* **2016**, *84*, 37–48. [[CrossRef](#)]
39. Amin, M.T.; Alazba, A.A.; Shafiq, M. Removal of Copper and Lead Using Banana Biochar in Batch Adsorption Systems: Isotherms and Kinetic Studies. *Arab. J. Sci. Eng.* **2017**, 1–12. [[CrossRef](#)]
40. Rajput, M.S.; Sharma, A.; Sharma, S.; Verma, S. Removal of Lead (II) from Aqueous Solutions by Orange Peel. *Int. J. Appl. Res.* **2015**, *1*, 411–413.

41. Ahmad, M.; Ahmad, M.; Usman, A.R.A.; Al-Faraj, A.S.; Abduljabbar, A.S.; Al-Wabel, M.I. Biochar Composites with Nano Zerovalent Iron and Eggshell Powder for Nitrate Removal from Aqueous Solution with Coexisting Chloride Ions. *Environ. Sci. Pollut. Res. Int.* **2017**. [[CrossRef](#)]
42. Usman, A.R.A.; Abduljabbar, A.; Vithanage, M.; Ok, Y.S.; Ahmad, M.; Ahmad, M.; Elfaki, J.; Abdulazeem, S.S.; Al-Wabel, M.I. Biochar Production from Date Palm Waste: Charring Temperature Induced Changes in Composition and Surface Chemistry. *J. Anal. Appl. Pyrolysis* **2015**, *115*, 392–400. [[CrossRef](#)]
43. Doğan, M.; Alkan, M.; Demirbaş, Ö.; Özdemir, Y.; Özmetin, C. Adsorption Kinetics of Maxilon Blue GRL onto Sepiolite from Aqueous Solutions. *Chem. Eng. J.* **2006**, *124*, 89–101. [[CrossRef](#)]
44. Gunay, A. Application of Nonlinear Regression Analysis for Ammonium Exchange by Natural (Bigadiç) Clinoptilolite. *J. Hazard. Mater.* **2007**, *148*, 708–713. [[CrossRef](#)]
45. Manohar, D.M.; Noeline, B.F.; Anirudhan, T.S. Adsorption Performance of Al-Pillared Bentonite Clay for the Removal of Cobalt(II) from Aqueous Phase. *Appl. Clay Sci.* **2006**, *31*, 194–206. [[CrossRef](#)]
46. Zaghouane-Boudiaf, H.; Boutahala, M.; Arab, L. Removal of Methyl Orange from Aqueous Solution by Uncalcined and Calcined MgNiAl Layered Double Hydroxides (LDHs). *Chem. Eng. J.* **2012**, *187*, 142–149. [[CrossRef](#)]
47. Rajoriya, R.K.; Prasad, B.; Mishra, I.M.; Wasewar, K.L. Adsorption of Benzaldehyde on Granular Activated Carbon: Kinetics, Equilibrium, and Thermodynamic. *Chem. Biochem. Eng. Q.* **2007**, *21*, 219–226.
48. Tang, H.; Zhou, W.; Zhang, L. Adsorption Isotherms and Kinetics Studies of Malachite Green on Chitin Hydrogels. *J. Hazard. Mater.* **2012**, *209–210*, 218–225. [[CrossRef](#)] [[PubMed](#)]
49. Chowdhury, S.; Mishra, R.; Saha, P.; Kushwaha, P. Adsorption Thermodynamics, Kinetics and Isothermic Heat of Adsorption of Malachite Green onto Chemically Modified Rice Husk. *Desalination* **2011**, *265*, 159–168. [[CrossRef](#)]
50. Taty-Costodes, V.C.; Fauduet, H.; Porte, C.; Delacroix, A. Removal of Cd(II) and Pb(II) Ions, from Aqueous Solutions, by Adsorption onto Sawdust of Pinus Sylvestris. *J. Hazard. Mater.* **2003**, *105*, 121–142. [[CrossRef](#)] [[PubMed](#)]
51. Hamdaoui, O. Dynamic Sorption of Methylene Blue by Cedar Sawdust and Crushed Brick in Fixed Bed Columns. *J. Hazard. Mater.* **2006**, *138*, 293–303. [[CrossRef](#)]
52. Liu, Z.; Zhang, F.-S. Removal of Lead from Water Using Biochars Prepared from Hydrothermal Liquefaction of Biomass. *J. Hazard. Mater.* **2009**, *167*, 933–939. [[CrossRef](#)]
53. Mahdi, Z.; Yu, Q.J.; El Hanandeh, A. Removal of Lead(II) from Aqueous Solution Using Date Seed-Derived Biochar: Batch and Column Studies. *Appl. Water Sci.* **2018**, *8*, 181. [[CrossRef](#)]
54. Yakkala, K.; Yu, M.-R.; Roh, H.; Yang, J.-K.; Chang, Y.-Y. Buffalo Weed (*Ambrosia Trifida* L. Var. *Trifida*) Biochar for Cadmium (II) and Lead (II) Adsorption in Single and Mixed System. *Desalination Water Treat.* **2013**, *51*, 7732–7745. [[CrossRef](#)]
55. Hu, X.; Xue, Y.; Liu, L.; Zeng, Y.; Long, L. Preparation and Characterization of Na₂S-Modified Biochar for Nickel Removal. *Environ. Sci. Pollut. Res.* **2018**, *25*, 9887–9895. [[CrossRef](#)] [[PubMed](#)]
56. Lyu, H.; Gao, B.; He, F.; Zimmerman, A.R.; Ding, C.; Huang, H.; Tang, J. Effects of Ball Milling on the Physicochemical and Sorptive Properties of Biochar: Experimental Observations and Governing Mechanisms. *Environ. Pollut.* **2018**, *233*, 54–63. [[CrossRef](#)]
57. Aksu, Z.; Tezer, S. Exploited Application of *Bacillus* Sp. ETL-A & *Pseudomonas* Sp. ETL-B in Microbial Degradation of Orange 16 Dye. *Process. Biochem.* **2001**, *36*, 431–439.
58. Chiou, M.S.; Li, H.Y. Equilibrium and Kinetic Modeling of Adsorption of Reactive Dye on Cross-Linked Chitosan Beads. *J. Hazard. Mater.* **2002**, *93*, 233–248. [[CrossRef](#)]
59. Mestre, A.S.; Pires, J.; Nogueira, J.M.F.; Carvalho, A.P. Activated Carbons for the Adsorption of Ibuprofen. *Carbon* **2007**, *45*, 1979–1988. [[CrossRef](#)]
60. Önal, Y.; Akmil-Başar, C.; Sarıcı-Özdemir, Ç. Elucidation of the Naproxen Sodium Adsorption onto Activated Carbon Prepared from Waste Apricot: Kinetic, Equilibrium and Thermodynamic Characterization. *J. Hazard. Mater.* **2007**, *148*, 727–734. [[CrossRef](#)]
61. Hamdaoui, O.; Naffrechoux, E. Modeling of Adsorption Isotherms of Phenol and Chlorophenols onto Granular Activated Carbon: Part I. Two-Parameter Models and Equations Allowing Determination of Thermodynamic Parameters. *J. Hazard. Mater.* **2007**, *147*, 381–394. [[CrossRef](#)]
62. Baccar, R.; Sarrà, M.; Bouzid, J.; Feki, M.; Blánquez, P. Removal of Pharmaceutical Compounds by Activated Carbon Prepared from Agricultural By-Product. *Chem. Eng. J.* **2012**, *211–212*, 310–317. [[CrossRef](#)]
63. Tan, I.A.W.; Ahmad, A.L.; Hameed, B.H. Adsorption Isotherms, Kinetics, Thermodynamics and Desorption Studies of 2,4,6-Trichlorophenol on Oil Palm Empty Fruit Bunch-Based Activated Carbon. *J. Hazard. Mater.* **2009**, *164*, 473–482. [[CrossRef](#)]
64. Foo, K.Y.; Hameed, B.H. Preparation, Characterization and Evaluation of Adsorptive Properties of Orange Peel Based Activated Carbon via Microwave Induced K₂CO₃ Activation. *Bioresour. Technol.* **2012**, *104*, 679–686. [[CrossRef](#)]
65. Malik, P.K. Use of Activated Carbons Prepared from Sawdust and Rice-Husk for Adsorption of Acid Dyes: A Case Study of Acid Yellow 36. *Dyes Pigment.* **2003**, *56*, 239–249. [[CrossRef](#)]
66. Kumar, P.S.; Ramakrishnan, K.; Gayathri, R. Removal of Nickel(II) from Aqueous Solutions by Ceralite IR 120 Cationic Exchange Resins. *J. Eng. Sci. Technol.* **2010**, *5*, 232–243.

-
67. Ramadoss, R.; Subramaniam, D. Removal of Divalent Nickel from Aqueous Solution Using Blue-Green Marine Algae: Adsorption Modeling and Applicability of Various Isotherm Models. *Sep. Sci. Technol.* **2019**, *54*, 943–961. [[CrossRef](#)]
 68. Saadi, R.; Saadi, Z.; Fazaeli, R. Determination of Axial Dispersion and Overall Mass Transfer Coefficients for Ni (II) Adsorption on Nanostructured γ -Alumina in a Fixed Bed Column: Experimental and Modeling Studies. *Desalination Water Treat.* **2015**, *53*, 2193–2203. [[CrossRef](#)]